Journal of Controlled Release 387 (2025) 114184

Contents lists available at ScienceDirect

Journal of Controlled Release

journal homepage: www.elsevier.com/locate/jconrel

Picoliter ice particles by supersonic cryogenic jets for transdermal drug delivery: Extracellular vesicle application for skin diseases

Hyunjoon Son [a,1], Sejong Kim [b,c,1], Kyung Min Lim [b], Daejin Kim [a], Kwonwoo Song [b], Myeongjin Song [b], Youngseo Lee [c], Sujin Yu [c], Daehyun Kim [d], Ssang-Goo Cho [b,c,*], Gun-Ho Kim [a,d,*]

[a] Department of Mechanical Engineering, Ulsan National Institute of Science and Technology, UNIST-gil 50, Ulsan 44919, Republic of Korea
[b] R&D Team, StemExOne Co., Ltd., Gwangjin-gu, Seoul 05029, Republic of Korea
[c] Department of Stem Cell and Regenerative Biotechnology, School of Advanced Biotechnology, Molecular & Cellular Reprogramming Center, Institute of Advanced Regenerative Science, and Institute of Health, Aging & Society, Konkuk University, Seoul 05029, Republic of Korea
[d] RecensMedical, Hwaseong 18468, Republic of Korea

ARTICLE INFO

Keywords:
Transdermal drug delivery
Small-volume needle-free drug delivery
Picoliter ice particle delivery (PIPD) technology
Extracellular vesicles
Anti-inflammatory
Regeneration

ABSTRACT

Transdermal drug delivery holds significant potential for treating skin conditions. Conventional methods utilizing needles or large unit drug delivery volumes often result in patient discomfort and inhomogeneous delivery. This study proposes a picoliter ice particle delivery (PIPD) technology that produces high-speed solid ice drug particles using controlled supersonic cryogenic jets for transdermal drug delivery. The proposed PIPD system simultaneously atomizes liquid drug to micro-droplets, freezes them to solid ice particles, and accelerates these particles to penetrate the skin barrier. All these processes occur within 300 μs, ensuring drug integrity. Notably, most of the particles exhibited volumes even below 1 picoliter. The average delivery efficiency of PIPD was found to be 50 % when used with ex vivo porcine skin, and in vivo mouse experiments suggest that PIPD's delivery efficiency to the dermis layer is comparable to traditional injection delivery. Stem cell-derived functional extracellular vesicles (EVs) did not show any reduction in their anti-inflammatory and regenerative cell absorption properties after PIPD. Consequently, PIPD EVs delivery led to significant therapeutic improvements in the wound and atopic dermatitis animal models.

1. Introduction

Transdermal drug delivery is increasingly recognized as an alternative to oral administration and needle-injection, given its capability of targeted delivery of drugs, minimizing side effects on other organs and ensuring efficient drug delivery to skin lesions [1–3]. Microneedle patches coated or carried with specific drugs or cryo-microneedles made of drug itself have demonstrated their ability to treat various skin lesions [4–8]. Recently, high-pressure liquid jet produced by various energy sources showed an effective transdermal delivery of drugs without using a physical needle [9–11]. However, potential drug degradation by heat or UV exposure required for manufacturing microneedles and the melting nature of cryo-microneedles limit their broad clinical applications. The liquid form of the high-pressure jet delivery limits its penetration capability (i.e., low impact strength of the liquid phase compared to the solid phase), which requires a large unit delivery volume for effective penetration (e.g., 10 nL) [12]. Gas-powder injection technology, utilizing the solid form of freeze-dried drug powders, provides superior penetration capability but has limitations related to the necessary powder preparation and the types of applicable drugs [13–16]. For these drug delivery methods, the unit delivery volume must be minimized for achieving uniform drug distribution and enhancing patient comfort; however, advancements in this area have primarily been confined to nanoliter scale due to technological challenges. In particular, jet drug delivery methods require long treatment durations due to the sequential delivery of individual drug particles [17]. Therefore, there is a lack of transdermal drug delivery methods that can simultaneously ensure patient comfort and clinical utility while minimizing the limitations imposed by surface conditions, pre-processing requirements, and degradation during manufacturing and delivery.

* Corresponding authors.
E-mail addresses: ssangoo@konkuk.ac.kr (S.-G. Cho), gunhokim@unist.ac.kr (G.-H. Kim).
[1] These authors contributed equally: Hyunjoon Son, Sejong Kim

https://doi.org/10.1016/j.jconrel.2025.114184
Received 23 May 2025; Received in revised form 14 August 2025; Accepted 30 August 2025
Available online 1 September 2025

A cryogenic jet delivers at extremely cold temperatures and supersonic speeds, resulting from the adiabatic expansion of highly pressurized cryogenic fluids. For instance, liquid carbon dioxide maintained at 50–70 bar at room temperature (RT) generates dry ice particles at −78.5 °C and produces a supersonic jet traveling at Mach 1 or higher. These properties make cryogenic jets ideal for converting liquid drugs into solid ice micro-particles at high velocities, which can physically penetrate the skin barrier and release the drugs as they melt due to body heat. However, insufficient temperature control in conventional cryogenic jets (e.g., liquid nitrogen spray) has limited their application in drug delivery due to the risk of thermal damage to target tissues, confining their use mainly to producing freeze-dried drugs or accelerating pre-formed powders [18,19].

This study presents a novel drug delivery system, namely picoliter ice particle delivery (PIPD), which utilizes a supersonic cryogenic jet to produce ice picoliter particles for the transdermal delivery of a wide range of drugs (Fig. 1). The high-speed jet atomizes the liquid drug into micro-sized droplets (i.e., picoliter volume), which are instantly frozen into solid ice particles by the adjacent cryogenic stream and simultaneously accelerated to high velocities. The solid ice particles generated in this process exhibit significantly higher impact pressures—up to several hundred times greater—than liquid droplets under identical conditions (e.g., mass, velocity), since solid particles remain undeformed during impact, and the impact time remains short [20]. This superior impact characteristic of solid ice particles allows effective skin penetration even with diameters more than tenfold smaller than 100 μm a size generally reported as pain-free [21]. Additionally, the rapid freezing and melting processes occurring within hundreds of microseconds prevent protein denaturation, osmotic imbalance and intracellular water migration, and ice crystal formation, thereby preserving the structural and biochemical integrity of the drug and ensuring its effectiveness. This pain-free picoliter-scale drug ice particles delivery without complex pre-processing or drug degradation by PIPD provides a versatile platform to overcome the inherent limitations of existing needle-free drug delivery technologies.

Ultimately, the intrinsic advantages of the PIPD system, together with our findings on the effective delivery of fragile biologics such as stem cell-derived extracellular vesicles (EVs), highlight its potential as a versatile platform for expanding drug delivery beyond simple skin targets to more challenging tissues, such as the eye. Moreover, this system broadens the scope of deliverable therapeutics to include sensitive drugs that are typically prone to degradation during conventional delivery processes, paving the way for next-generation therapeutic applications.

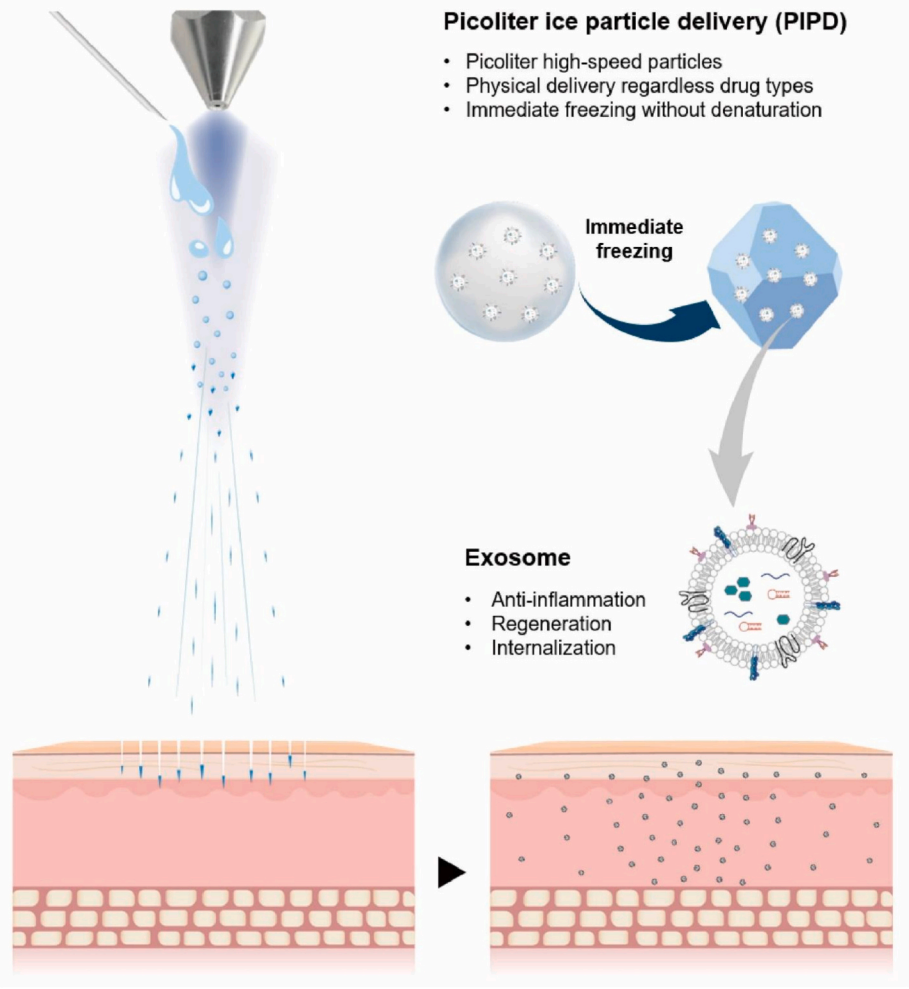

Fig. 1. Schematic representation and significant advantages of PIPD and exosome. The supplied drug undergoes simultaneous atomization and freezing within a microsecond scale via a supersonic cryogenic jet, resulting in the formation of picoliter-scale drug ice particles. These ice particles, preserved in their solid state due to the low jet temperature, penetrate the stratum corneum, the toughest barrier of the skin. Upon reaching the epidermis, the ice particles melt, releasing exosomes with anti-inflammatory and regenerative properties, which are then homogeneously distributed across the entire dermis layer.

2. Results

2.1. Selection of a cryogenic medium for jet temperature control

The thermodynamic properties (e.g., pressure and temperature) of a cryogenic substance were controlled by a rapid heat exchange module before its adiabatic expansion to 1 atm using a precision cooling device produced by RecensMedical, Inc. Liquid carbon dioxide was employed, with its enthalpy adjusted to regulate the liquid/gas ratio, thereby controlling the jet temperature (Supplementary Fig. 1). The average enthalpy of carbon dioxide controlled by the system was approximately 600 kJ/kg ($\Delta h \approx 40$ kJ/kg), and the final jet temperature upon reaching the skin for ice particle preservation was approximately −3 °C (Fig. 2A). This jet temperature is within a safe range for short-term exposure, posing no risk of thermal damage to the skin. These final jet temperatures were measured using a T-type thermocouple with 0.8 mm diameter, positioned 10 mm away from the nozzle orifice.

2.2. Ice particle formation mechanism

When the liquid drug is introduced into a supersonic cryogenic jet, the negative pressure created by the high-speed jet pulls the liquid drug to the jet core. Once the drug is exposed to the jet, it undergoes a primary breakup which determines the initial droplet size and subsequently undergoes a secondary breakup which forms tiny droplets. This atomization process is influenced by the drug's properties, such as density and surface tension, viscosity, as well as its relative velocity to the jet [22–24], ultimately resulting in picoliter-scale liquid particles (Fig. 2C).

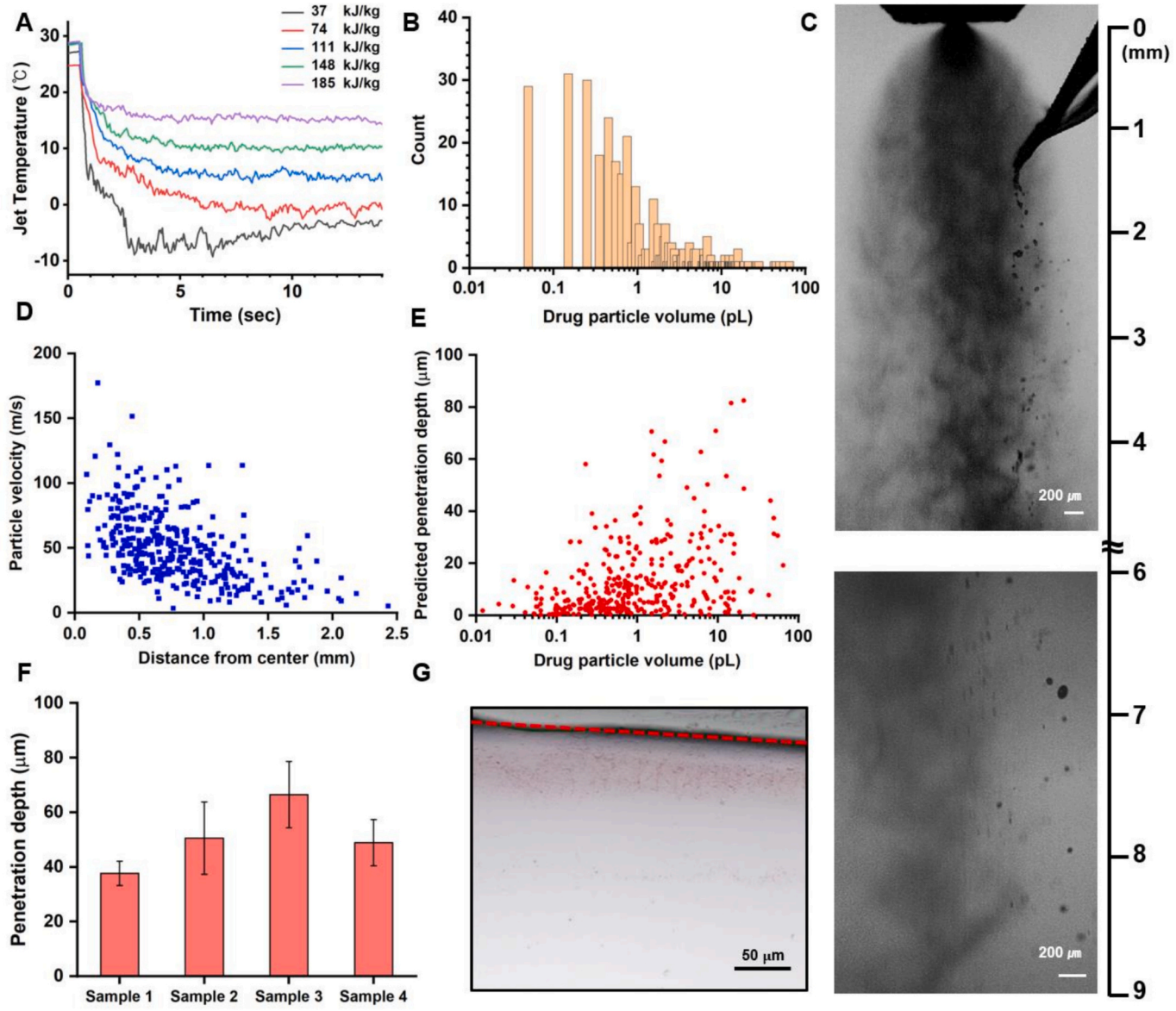

Fig. 2. Characterization of particle behavior and penetration depth in the PIPD system. (A) Jet temperature over time at a 10 mm distance from the nozzle, with curves corresponding to different enthalpy increase levels. (B) Volume distribution of the delivering drug particles. (C) High-speed camera images of the initial atomization process of the injected drug, showing the primary breakup of the liquid drug, the early stages of secondary breakup, and final atomization process between 6 and 9 mm from the nozzle (shutter speed: 750 ns). (D) Velocity of drug particles at distances from the jet centerline (E) Predicted drug penetration depth based on drug particle volume. (F) Experimental penetration depth in four gelatin model samples immediately after delivery with the PIPD system, with five measurement regions per sample. The drug was mixed with 0.5 μm carboxylated red-dyed microspheres before delivery for visualization. (G) Microscopic image showing the physical penetration depth into a gelatin model. Red dashed lines indicate top surface boundary. (For interpretation of the references to colour in this figure legend, the reader is referred to the web version of this article.)

Following the atomization process, the drug droplets undergo thermal exchange with the surrounding cryogenic jet and freeze into ice particles. The heat exchange calculation process for ice particle formation is provided in the Supplementary Information.

The freezing time is estimated to be within 300 μs, which is significantly faster than the onset of cell volume changes due to the osmotic pressure in water (~50 ms) and the liposome solution exchange time (~10 ms) reported in previous studies [25]. Such a rapid freezing process removes the risk of osmotic damage to cells and cell-based drugs. Furthermore, the freezing time is faster than the slow rearrangement time of protein side chains (3–10 ms) [26]. These results suggest that the freezing process of PIPD can effectively preserve the structural integrity of cell or protein-based drugs. Specifically, when the volume of a single particle decreases below 1 pL, the freezing time for most particles falls below 100 μs (Supplementary Fig. 2C). In this study, the drug was injected 1 mm vertically and 0.5 mm horizontally from the nozzle orifice, at a flow rate of 500 μL/min.

2.3. Skin penetration mechanism

When the drug, transformed into ice particles, is ejected in solid form toward the skin, it penetrates upon collision, with minimal particle deformation and energy dissipation due to the short impact duration. Most kinetic energy of the ice particle before reaching the skin is converted to work that enables skin penetration. In this study, the skin's resistance stress σ_b to predict the penetration behavior was set to 1 MPa based on the findings by Mitchell in micro-particle ballistic penetration [27,28]. Since this penetration process time (t_f) is more than 100 times shorter than the time of particle melting (t_p), the particle volume changes due to heat exchange were negligible during skin penetration. Moreover, it is worth noting that this extremely short melting time within the skin minimizes the impact of the melting process on the drug integrity (Supplementary Fig. 2C).

2.4. Behavior and penetration analysis of drug particles

This study analyzed the relationship between the velocity and volume of ice particles to estimate their kinetic energy and predict the penetration depth. The analysis revealed that most particle volumes were below 1 pL (Fig. 2B), and the velocity of the ice particles was more influenced by the force exerted by the cryogenic jet than by their volume. Generally, particles closer to the center of the jet exhibited higher velocities, indicating a stronger force concentration (Fig. 2D). Across a particle size and volume range of 0.01–10 pL, the particles were observed to travel at approximately 100 m/s. These findings suggest that the cryogenic jet effectively accelerates the particles, enabling efficient drug delivery while minimizing skin damage due to low kinetic energy and enhanced penetration efficiency from the rigid particles.

Additionally, the predicted penetration depth based on the kinetic energy was found to increase with the particle volume (Fig. 2E). These results exhibit a correlation similar to that observed in previous studies between particle volume and penetration depth. Notably, they suggest the potential for more precise drug delivery using pL-scale drug particle volumes, which have been challenging to achieve with conventional needle-free transdermal delivery technologies based on physical mechanisms (Fig. 3). Detailed explanations and calculations of the drug penetration process are provided in the Supplementary Information.

To experimentally predict the initial penetration depth in the skin, a gelatin model with hardness similar to that of human skin was used [29–31]. While the gelatin model does not fully replicate the micromechanical properties of actual human skin, it provides a controlled medium for studying penetration. The mechanical properties of human or pig skin, such as resistance stress and stiffness, vary depending on temperature, humidity, and tensile direction. These factors influence the ballistic delivery of microparticles and the resulting penetration depth. The thickness of stratum corneum also critically affects the final penetration depth. [32–34]. The gelatin model was employed to minimize and control such variations in sample properties. Under identical drug delivery conditions, penetration depth data were collected from four gelatin samples, each with five measurements. The initial penetration depth in the gelatin model was 50.89 μm (SE = 3.15 μm; SD = 14.1 μm) (Fig. 2F, G). While the RSD is moderately above the commonly referenced 10–20 % range for reproducible delivery systems, the relatively small SE indicates that the mean penetration depth was consistent across samples, reflecting a high degree of parallel stability in the system's delivery performance.

To evaluate dermal penetration efficiency in vivo, DiR-labeled EVs were delivered using different application methods (Fig. 4A) into mouse dorsal skin tissues, an established model used in early-stage transdermal delivery studies for its accessibility, reproducibility, and suitability for

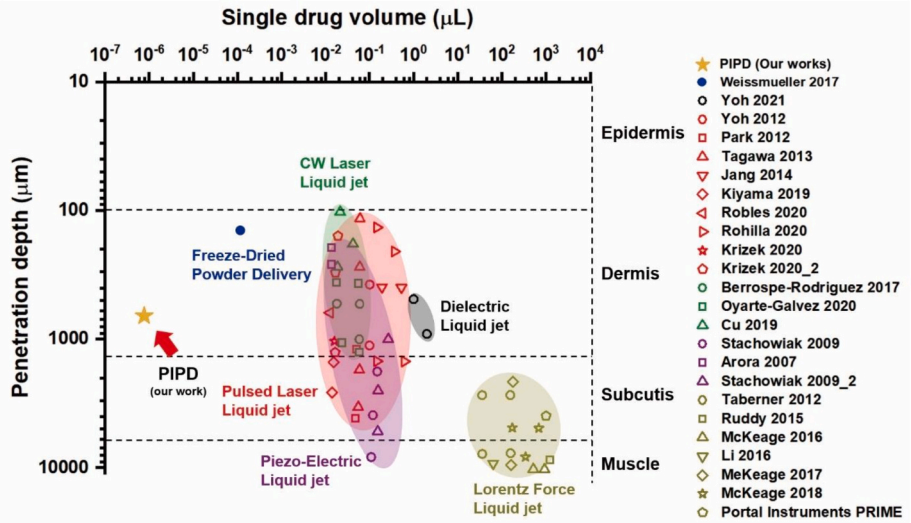

Fig. 3. Comparison of penetration depth distributions for a single drug delivery volume across various physical drug delivery technologies. For PIPD, the penetration depth was assessed in vivo in mice 24 h post-administration using confocal microscopy images. For freeze-dried powder delivery, the penetration depth represents the expected depth in the mouse skin following gas-powder injection. Notably, 28 days post-administration, the freeze-dried powder was observed to have spread intradermally. The outlined values represent experimental penetration depths confirmed after a sufficient diffusion period for liquid-based injection jet technologies, performed using various injection mechanisms.

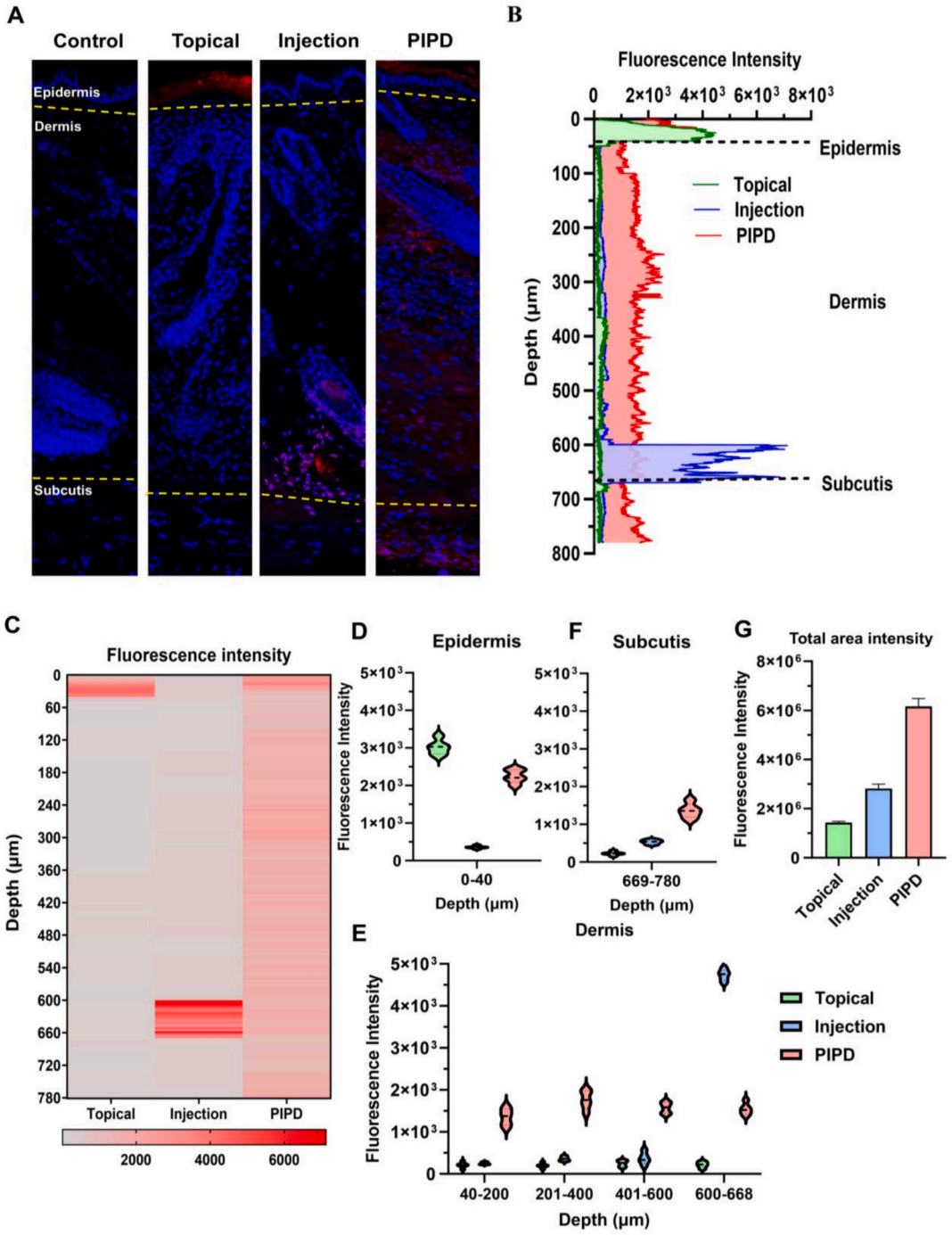

Fig. 4. Comparative analysis of the tissue penetration and biodistribution of DiR-labeled EVs using different delivery methods. (A) Representative confocal microscopy images showing the distribution of DiR-labeled EVs (red) in mouse dorsal skin. The cell nuclei were counterstained with DAPI (blue). The yellow dotted lines indicate the boundaries between different skin layers. (B) Quantitative depth-dependent fluorescence intensity profiles across skin layers for different delivery methods. (C) Heat map visualization of fluorescence intensity distribution across skin depths for topical, injection, and PIPD delivery methods. (D—F) Layer-specific quantification of fluorescence intensity in (D) epidermis (0–40 μm), (E) dermis (40–668 μm), and (F) subcutis (669–780 μm). (G) Total area fluorescence intensity on image comparison among different delivery methods. ****$p < 0.0001$. (For interpretation of the references to colour in this figure legend, the reader is referred to the web version of this article.)

controlled experimental evaluation [35,36]. Notably, confocal microscopy revealed distinct penetration patterns in the skin tissue. The topical application resulted in fluorescence signals predominantly confined to the epidermal layer, with limited deeper penetration. Conversely, injection delivery showed intense localized fluorescence in the subcutaneous layer, whereas PIPD achieved uniform distribution across all skin layers (Fig. 4A). A depth-dependent fluorescence intensity profiling further quantified these differences (Fig. 4B). The topical application exhibited high fluorescence intensity but remained restricted to the epidermis, while injection showed concentrated signals in the subcutaneous layer. In contrast, PIPD demonstrated consistent fluorescence across all layers up to 780-μm depth. A heat map visualization confirmed these distribution patterns: superficial distribution for topical, localized signals at specific depths for injection, and

comprehensive tissue distribution for PIPD (Fig. 4C). The quantitative analysis of dermal regions revealed consistent fluorescence intensity in PIPD compared to the limited penetration in topical and injection (Fig. 4D–F). The total fluorescence intensity analysis showed significantly enhanced delivery efficiency with PIPD compared to that with injection and topical application (Fig. 4G). The total administered dose of EVs was consistent across all delivery methods to allow direct comparison (i.e., 500 μL). It is worth to note that the total area intensity of the PIPD group after 24 h was found to be greater than that of the traditional injection delivery (Fig. 4G). We attribute this to the fact that the EVs by a 30 g needle was injected directly to the dermis layer where active blood flow removes foreign materials whereas EVs by PIPD were firstly delivered to the epidermis layer that lacks active blood flow (Fig. 2E) and slowly diffused to the deeper layer during the 24 h.

These findings demonstrate that topical application is limited by physical constraints like exosome size and biomembrane permeability [37]. While injection achieves localized accumulation in the subcutaneous tissue, therapeutic effects may remain restricted to specific

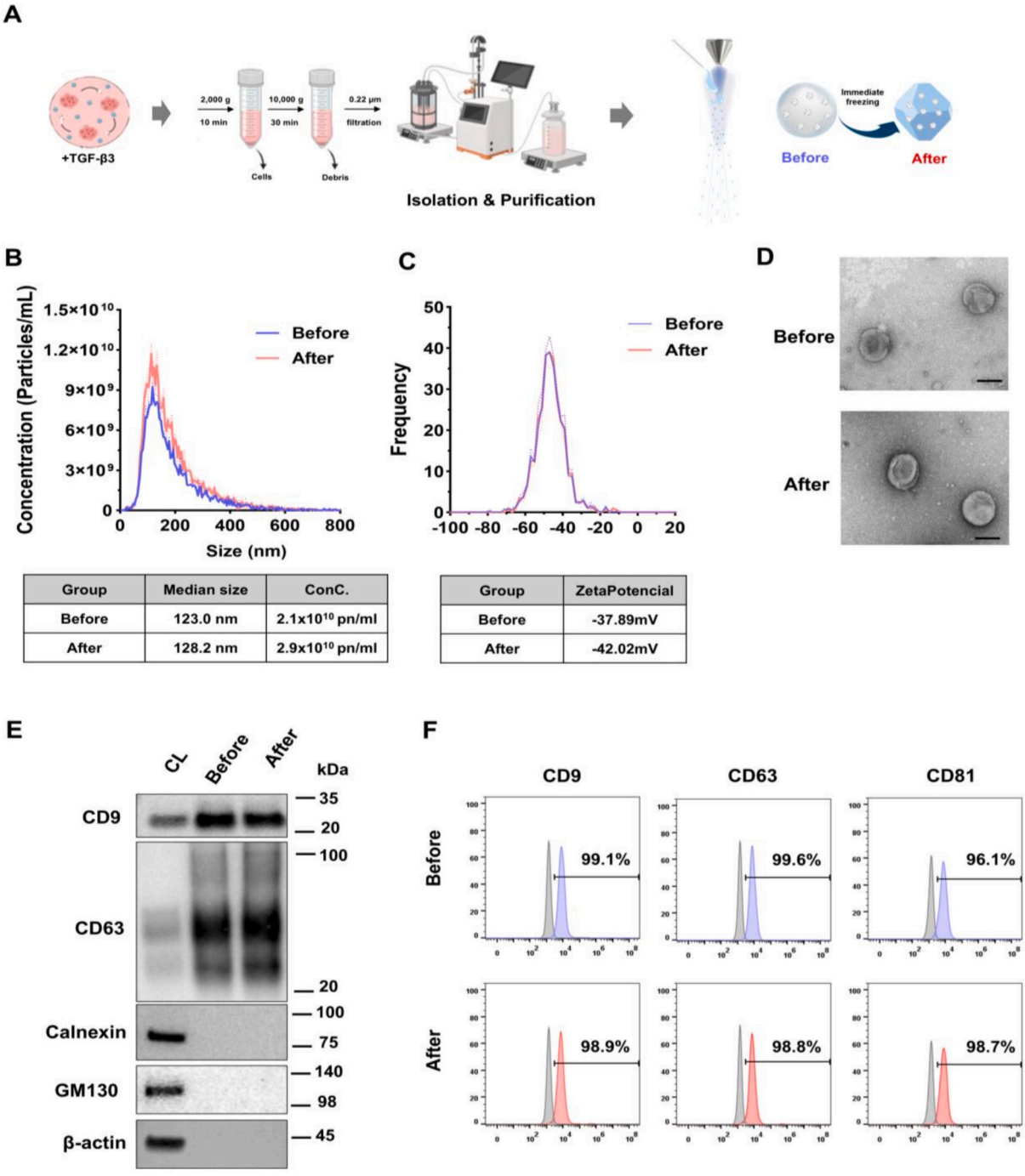

Group	Median size	ConC.
Before	123.0 nm	2.1x10¹⁰ pn/ml
After	128.2 nm	2.9x10¹⁰ pn/ml

Group	ZetaPotencial
Before	-37.89mV
After	-42.02mV

Fig. 5. Comprehensive characterization of EVs before and after PIPD. (A) Schematic illustration of EV isolation and purification process using the TFF system. (B) Size distribution analysis of EVs measured by NTA, showing particle concentration and size distribution before and after PIPD. (C) Zeta potential measurements demonstrating surface charge characteristics. (D) Representative TEM images showing morphological features. Scale bar = 100 nm. (E) Western blot analysis of EV positive markers (CD9, CD63) and negative markers (GM130, Calnexin), with β-actin as the loading control. (F) Flow cytometric analysis of surface markers (CD9, CD63, CD81) expression.

regions [38]. In contrast, PIPD enables uniform distribution across multiple skin layers while maintaining consistent therapeutic concentrations. This highlights its potential as an effective delivery platform for exosome-based therapeutics in dermatological applications [37]. Further studies are warranted to evaluate its efficiency with various therapeutic cargos and assess long-term safety through extended monitoring. The comprehensive tissue distribution achieved by PIPD underscores its promise as a novel alternative to conventional delivery methods.

2.5. Characterization and functional preservation of EV before and after PIPD system

The EVs were produced from WJ-MSC using previously established methods [39,40], and their characteristics were analyzed before and after PIPD to evaluate its impact on EV properties (Fig. 5A). Nanoparticle tracking analysis revealed similar size distributions between the two groups, with median diameters of 123.0 nm (before) and 128.2 nm (after). Particle concentrations were 2.1×10^{10} particles/mL before PIPD and 2.9×10^{10} particles/mL after PIPD, indicating that particle yield was preserved (Fig. 5B). Zeta potential measurements showed comparable surface charge values (−37.89 mV before, −42.02 mV after), confirming that colloidal stability was maintained after PIPD (Fig. 5C). Transmission electron microscopy demonstrated characteristic cup-shaped morphology and intact membrane structures in both groups, indicating that the vesicular architecture was preserved (Fig. 5D). Western blot analysis confirmed the presence of EV-specific markers CD9 and CD63 in both groups, while negative markers GM130 and Calnexin were not detected (Fig. 5E). Flow cytometry analysis showed high expression levels of canonical EV markers CD9, CD63, and CD81 in both groups, with no significant differences observed between before (99.1 %, 99.6 %, 96.1 %) and after PIPD (98.9 %, 98.8 %, 98.7 %) populations (Fig. 5F). These results demonstrate that the PIPD system effectively delivers EVs while preserving their physicochemical and biological properties.

To assess whether the biological activity of EVs is retained following the PIPD system, we conducted comparative in vitro analyses using before and after PIPD EVs. DiR-labeled EVs were incubated with HaCaT and HDF to assess cellular uptake. Confocal microscopy revealed robust internalization of EVs in both cell types, with no observable differences in fluorescence intensity or subcellular distribution between the two groups (Fig. 6A), indicating that PIPD does not compromise membrane integrity or uptake efficiency. Cell viability assays were performed using HaCaT and HDF cells treated with escalating concentrations of EVs. Both before and after PIPD EVs significantly enhanced the viability of these skin-derived cells compared to untreated controls, without significant differences between groups at any concentration (Fig. 6B). Given the key roles of HaCaT and HDF in skin regeneration and repair processes, these findings indicate that EVs processed via PIPD retain their potential efficacy for promoting skin regeneration and exerting anti-inflammatory effects. We next evaluated the anti-inflammatory function of EVs using RAW 264.7 cells stimulated with lipopolysaccharide (LPS). Quantitative RT-PCR (qRT-PCR) demonstrated that both before and after PIPD markedly suppressed the expression of key pro-inflammatory genes, including iNOS, IL-1β, and IL-6, to levels comparable to those achieved by dexamethasone (DEX) treatment (Fig. 6C). There were no significant differences in gene suppression efficacy between the two EV groups, indicating that PIPD does not affect the immunomodulatory capacity of EVs. In parallel, nitric oxide (NO) production was measured to further validate the anti-inflammatory effects. LPS stimulation significantly elevated NO levels, whereas treatment with both before and after PIPD at 1×10^8 and 1×10^9 particles/mL significantly reduced NO concentrations. No differences were observed between EVs before and after PIPD at either concentration, further supporting that PIPD preserves EV bioactivity at the functional level (Fig. 6D). Collectively, these findings demonstrate that PIPD processing does not impair EV uptake, proliferative effects, or anti-inflammatory activity. The retention of these functional properties suggests the utility of PIPD as a non-invasive delivery strategy for maintaining EV therapeutic efficacy in regenerative medicine and inflammatory disease contexts. It is worth to note that larger biologic particles experienced longer thermal stress during a freezing-thawing cycle and therefore are more prone to structural instability compared to smaller particles. The intact integrity of EVs after PIPD, which are approximately 100 nm in size and possess greater biological complexity than other biomolecules such as proteins or mRNA, indirectly suggests that other smaller and simpler drugs could likewise be effectively delivered by PIPD without change in drug integrity.

2.6. In vivo efficacy in wound and atopic dermatitis (AD) models

To assess the therapeutic efficacy of EVs delivered via PIPD system in promoting wound healing, a mouse dorsal wound healing model was utilized. Wound closure was systematically evaluated on days 0, 3, 5, 7, and 11 post-wounding, with final tissue harvesting conducted on day 12 (Fig. 7A). The wound closure progression was monitored through macroscopic images across all treatment groups (Fig. 7B). By day 11, wound closure in the topical demonstrated 92.15 % closure relative to the control. The injection exhibited 97.11 % closure, while the PIPD achieved the most significant improvement with 99.5 % closure. These data indicate that all treatments significantly outperformed the control in promoting wound healing, with PIPD demonstrating the highest efficacy (Fig. 7C, D). Histological analysis using hematoxylin and eosin (H&E) staining on day 12 revealed distinct tissue regeneration patterns among groups (Fig. 7E). Collagen fraction and tissue remodeling were assessed using Masson's trichrome (MT) staining (Fig. 7F). The topical showed moderate improvement with a tissue width of 1.8 ± 0.1 mm compared to the control (2.5 ± 0.3 mm). The injection exhibited enhanced regeneration with a width of 1.2 ± 0.2 mm, while the PIPD demonstrated superior healing with the smallest tissue width at 0.8 ± 0.2 mm (Fig. 7G). The collagen fraction in wound tissues was analyzed, showing that the topical demonstrated a moderate collagen fraction (70.19 ± 9.22 %), which was not significantly different from the control (65.57 ± 11.46 %). The injection exhibited collagen synthesis (43.25 ± 4.45 %), while the PIPD showed comparable collagen fractions (39.88 ± 6.07 %) to the injection, with no statistically significant differences between these two groups (Fig. 7H). Although macroscopic wound closure rates did not differ significantly between the PIPD and injection groups (Fig. 7D), histological analysis on day 12 showed a significantly smaller tissue width in the PIPD group than in the topical and injection groups (Fig. 7G). These findings suggest that PIPD enabled uniform drug distribution across irregular lesion surfaces, which may have contributed to more advanced tissue regeneration.

Next, we investigated the anti-inflammatory and skin regenerative efficacy of EVs delivered via PIPD in a more complex AD mouse model induced by repeated application of 2 % 2,4-dinitrochlorobenzene (DNCB). EV treatments were administered using topical, injection, and PIPD, followed by comprehensive assessments on days 7, 14, and 21 post-treatment. The AD severity was assessed using established scoring systems based on erythema, hemorrhage, scarring, dryness, excoriation, and erosion, as described in previous studies of atopic dermatitis models [41,42]. Among the treatment groups, PIPD significantly reduced all AD-related scores to levels comparable to the injection, while topical also resulted in notable score reduction (Fig. 8A–C). Representative images of AD lesions at each time point further illustrate these improvements (Fig. 8B). Histological analysis on day 21 revealed significant reductions in epidermal thickness and mast cell infiltration in the PIPD group, comparable to the injection group (Fig. 8D–G). The topical treatment also decreased epidermal thickness but had limited effects on mast cell infiltration. H&E staining demonstrated improved tissue architecture in the PIPD and injection groups, while toluidine blue staining highlighted reduced mast cell density in these groups compared to

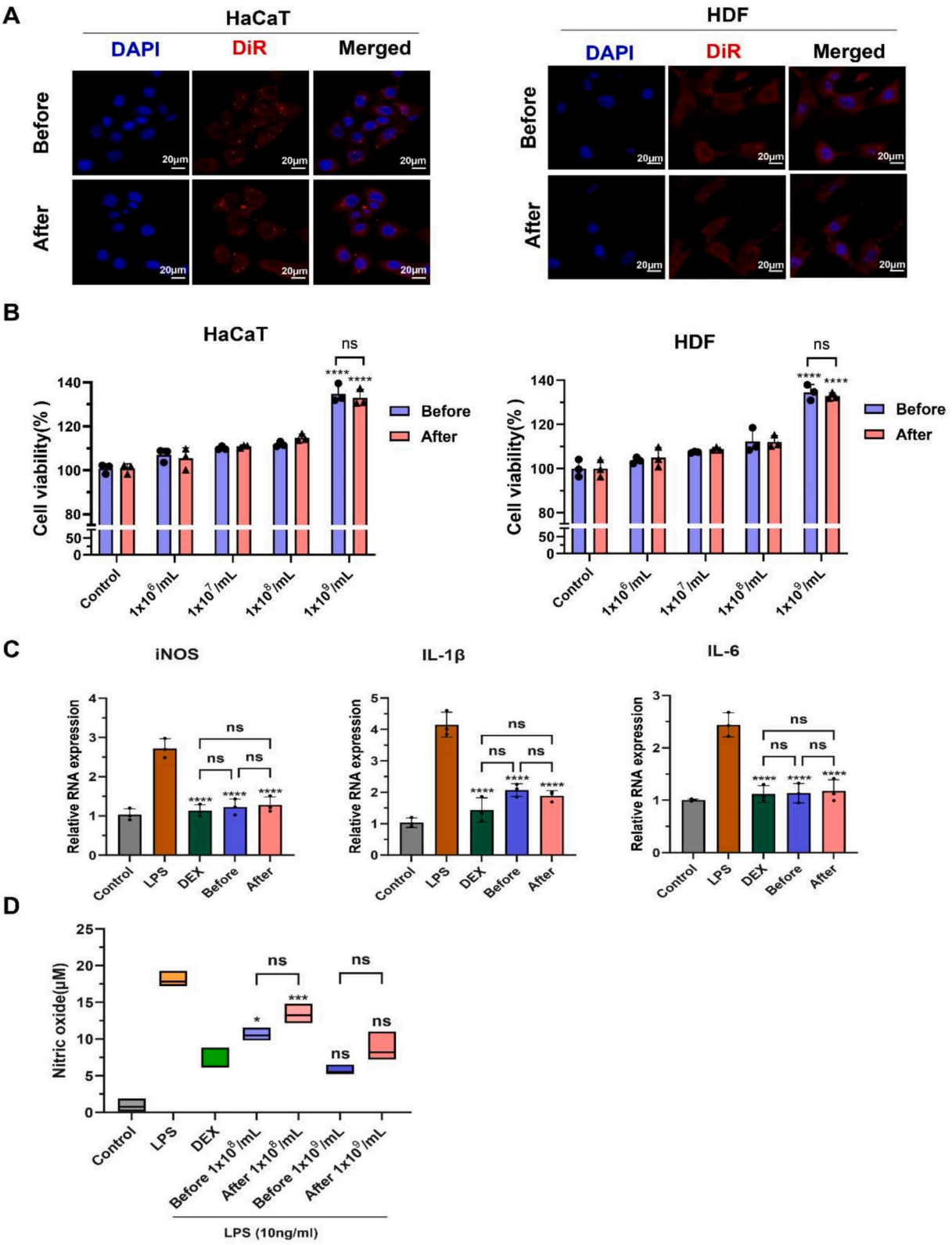

Fig. 6. Preservation of biological functionality of EV following PIPD. (A) Representative confocal microscopy images showing cellular uptake of DiR-labeled EVs (red) by HaCaT and HDF cells before and after PIPD. Nuclei were counterstained with DAPI (blue). Scale bars: 20 μm. (B) Quantification of cell viability in HaCaT and HDF cells treated with dose-dependent (1×10^6 to 1×10^9 particles/mL) of EVs before and after PIPD. ns: not significant; **** $p < 0.001$ compared to the control. (C) Relative mRNA expression levels of inflammatory markers assessed by qRT-PCR in LPS-stimulated RAW 264.7 cells following treatment with EVs before and after PIPD. DEX served as positive control. ns: not significant; **** $p < 0.001$ compared to the control. (D) NO production quantified by Griess assay in RAW 264.7 cells stimulated with LPS and treated with EVs before and after PIPD. ns: not significant; *$p < 0.05$; **** $p < 0.001$ compared to DEX. (For interpretation of the references to colour in this figure legend, the reader is referred to the web version of this article.)

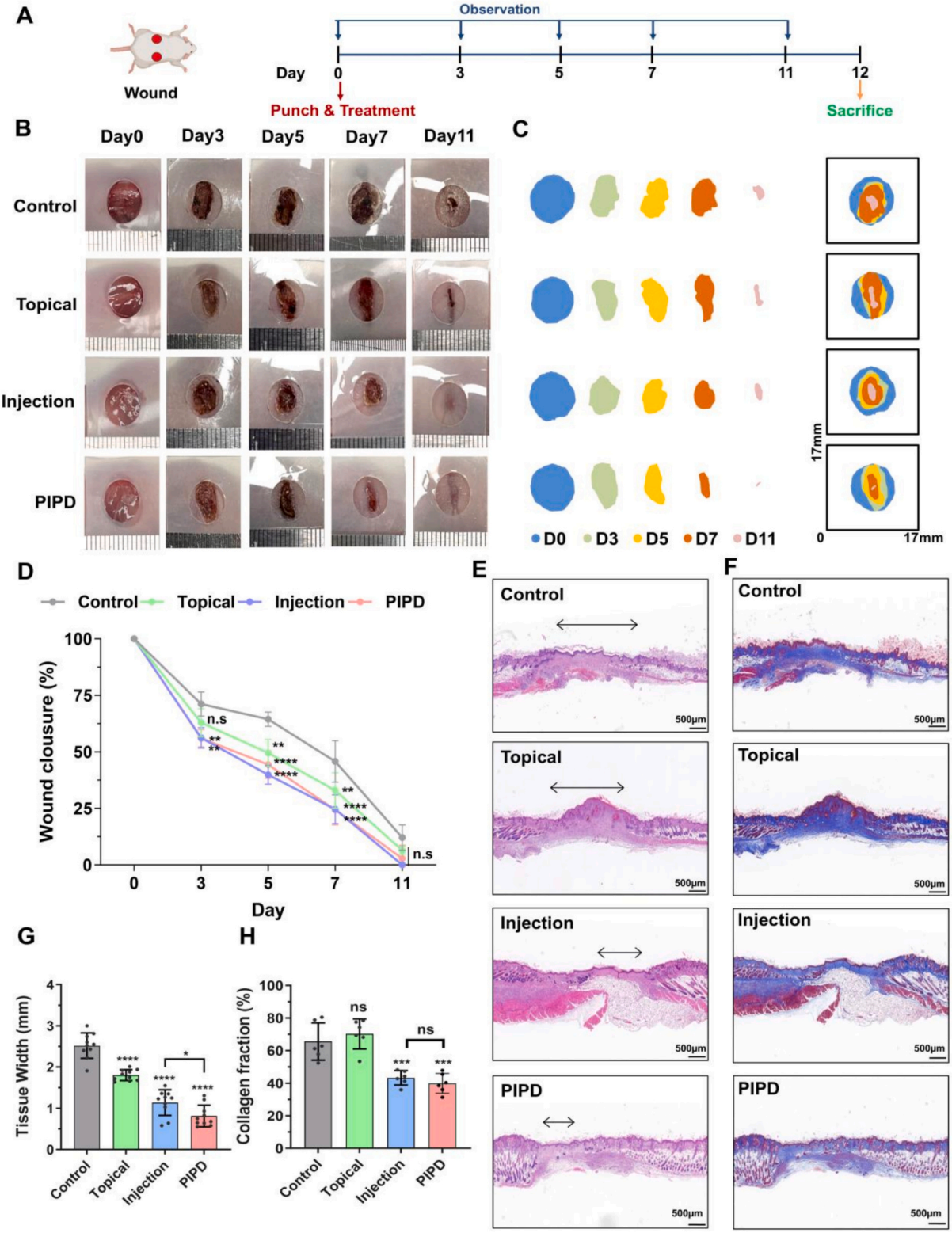

Fig. 7. Evaluation of wound healing efficacy using different EV deliveries. (A) Schematic illustration of the experimental timeline for wound healing assessment. (B) Representative macroscopic images of wound closure progression at days 0, 3, 5, 7, and 11 post-wounding across different treatment groups. (C) Wound closure trace. (D) Quantitative analysis of the wound closure rates over time. ns: not significant, $^{**}p < 0.01$; $^{****}p < 0.0001$ compared to the control (E) Representative H&E stained histological sections of wound sites on day 12. Scale bar = 500 μm. (F) Masson's trichrome staining of wound sections showing collagen deposition (blue) on day 12. Scale bar = 500 μm. (G) Quantitative analysis of the tissue width on day 12. $^{*}p < 0.01$; $^{****}p < 0.0001$ compared to the control (H) Quantification of the collagen deposition in wound sites on day 12. ns: not significant; $^{***}p < 0.001$ compared to the control. (For interpretation of the references to colour in this figure legend, the reader is referred to the web version of this article.)

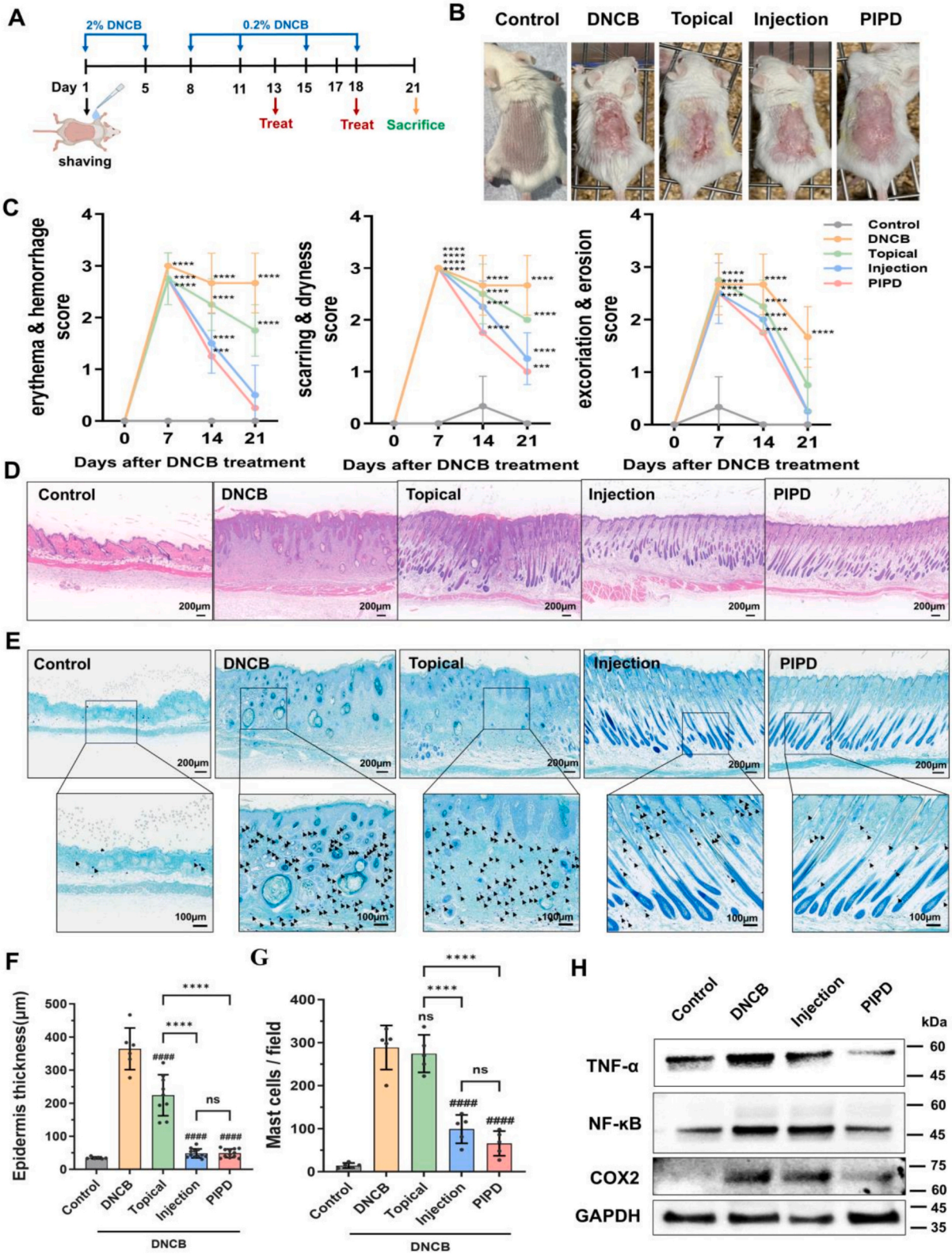

Fig. 8. Evaluation of the therapeutic effects using DNCB-induced atopic dermatitis mouse model. (A) Schematic illustration of the experimental timeline. (B) Representative macroscopic images of dorsal skin lesions across experimental groups (C) Clinical severity scores over 21 days showing erythema/hemorrhage, scarring/dryness, and excoriation/erosion among different groups. ****$p < 0.0001$ (D) Histological analysis of dorsal skin sections stained with H&E showing epidermal thickness. Scale bar = 200 μm. (E) Toluidine blue staining of skin sections showing mast cell infiltration (black arrows) Scale bar = 200 μm. Higher-magnification images of the boxed areas are shown below. Scale bar = 100 μm. (F) Quantitative analysis of epidermal thickness across different groups. ns: not significant, ****$p < 0.0001$; ####$p < 0.0001$ compared to DNCB. (G) Quantification of the mast cells per field of view in different groups. ns: not significant, ****$p < 0.0001$; ####$p < 0.0001$ compared to DNCB. (H) Western blot analysis of the inflammatory markers. (For interpretation of the references to colour in this figure legend, the reader is referred to the web version of this article.)

the controls. A quantitative analysis confirmed that PIPD achieved the most effective reduction in inflammatory markers among all treatments. To further elucidate the anti-inflammatory mechanisms, protein expression levels of critical inflammatory mediators were analyzed via Western blotting. The PIPD group exhibited the lowest expression levels of these proteins, indicating a robust suppression of the inflammatory pathways (Fig. 8H). These findings suggest that PIPD effectively delivers EVs to targeted skin layers, achieving therapeutic outcomes comparable to injection while surpassing topical delivery in both anti-inflammatory and regenerative effects. In summary, PIPD demonstrated significant efficacy in mitigating inflammation and promoting skin regeneration in an AD model. Its ability to reduce epidermal thickness, mast cell infiltration, and inflammatory protein expression highlights its potential as a promising EV delivery system for treating inflammatory skin disorders.

3. Discussion

EVs delivered via the PIPD systems retained full bioactivity, as demonstrated by their anti-inflammatory and regeneration effects in both wound healing and AD models (Figs. 7, 8). These therapeutic outcomes are attributed to the homogeneous dermal EV distribution achieved through ice particle-mediated delivery. Importantly, PIPD circumvents shear-induced EV lysis—a common limitation of liquid jet injections—by decoupling acceleration forces from payload integrity through cryogenic solidification. The observed collagen dynamics further support the ability of PIPD to modulate advanced stages of tissue repair (Fig. 7H). During the wound healing process, collagen is initially overproduced to provide structural integrity, followed by degradation or remodeling once the skin structure is restored [43,44]. The higher collagen deposition observed in the control and topical groups suggests that these treatments may correspond to earlier healing stages. In contrast, the injection and PIPD groups appear to have achieved faster progression to advanced healing phases, where collagen remodeling and normalization are more prominent. These results indicate that while all treatments promoted appropriate collagen deposition, PIPD achieved superior wound closure and tissue regeneration compared to topical and injection approaches. Notably, a single treatment required only 30 s, highlighting the system's efficiency in delivering therapeutic results. These findings suggests that the proposed PIPD is an effective and painless transdermal drug delivery method for a broad range of various protein and cell-based drugs.

In this work, while murine models provided mechanistic insights, interspecies differences in dermal stiffness necessitate caution in extrapolating penetration depths to clinical settings. For example, the human epidermis is approximately five times thicker than that of mice, with lower follicular density and greater mechanical stiffness, which reduces drug penetration [45,46]. In addition, humans possess a higher total amount of ceramides and a greater diversity of ceramide subclasses, forming a chemically stronger barrier [47,48], which suggests lower penetration performance under clinical conditions. Nevertheless, even in the highly permeable murine model, PIPD exhibited substantially better penetration performance compared to topical application and achieved a more homogeneous drug distribution than injection, underscoring the system's effectiveness in drug delivery.

To further evaluate the practical penetration capability of PIPD in a model more analogous to human skin, we conducted ex vivo experiments using porcine skin tissue (Franz Cell Membrane, APURES), which is widely used as a surrogate for human skin due to its comparable epidermal thickness, dermal structure, and mechanical properties [49,50]. These experiments confirmed that PIPD effectively penetrated porcine skin and demonstrated superior penetration performance under all tested conditions compared with topical application (Supplementary Fig. 3).

In the porcine skin experiments, the penetration efficiency—defined as the fraction of the administered drug that successfully penetrated the tissue during jet delivery—averaged 50 %, with a standard deviation of 7 %, corresponding to a relative standard deviation (RSD) of 14 %, which reflects the system's consistency (Supplementary Table 3). This RSD (14 %) falls within the 10–20 % reproducibility range typically required for transdermal drug delivery systems. Considering this value alongside the supplied flow rate, the system demonstrated a drug administration rate of approximately 250 μL/min. Nevertheless, this value is likely underestimated because a portion of the penetrated liquid drug was possibly diffused to a laboratory wiper used to remove any residual liquid on the surface. In addition, since the porcine skin was thermally isolated and rapidly chilled by PIPD, an ice layer on the surface was formed, which potentially blocks the following ice particles, as well as the porcine skin became more brittle at low temperatures. In contrast, the living skin is expected to remain warmer by body heat, preventing the formation of ice layer, maintaining its softness, and therefore leading to higher overall penetration efficiency of PIPD [32].

The parameters of the PIPD system in this study were selected to maintain the skin temperature within a safe range to prevent frostbite. For example, exposure to temperatures below −4 °C for more than four minutes has been reported to induce apoptosis of melanocytes [51]. To prevent such thermal damage, the cryogenic jet was controlled so that the skin surface temperature remained above −4 °C. Therefore, when targeting tissues with lower mechanical strength, greater susceptibility to thermal injury, or a high density of blood vessels, further optimization of parameters—including orifice size, cryogen energy input, and standoff distance—would be required. Furthermore, the particle size variability observed with high-viscosity formulations highlights the importance of system optimization—such as adjusting the drug supply rate or drug properties—as a critical engineering priority to ensure consistent dosing across diverse therapeutic payloads.

Based on previous reports and our in vivo observations showing no visible acute or delayed adverse reactions, PIPD appears to have acceptable tolerability; Our in vivo observations may provide supportive evidence of tolerability within the scope of our experiments. In the wound-healing model, no acute visible adverse reactions (e.g., erythema, edema, or exudation; Fig. 7B) were observed immediately after application on Day 0, and no delayed macroscopic changes were noted during the subsequent observation period. In the atopic dermatitis model, PIPD was not associated with additional visible injury on already inflamed skin at Day 0 (supplementary Fig. 4) and was accompanied by a reduction in clinical irritation scores (Fig. 8C), probably suggesting acceptable tolerability under our testing conditions. Regarding pain perception, pain-associated behaviors were not observed in either model following application. Further studies for formal assessments of skin barrier integrity, irritation, or pain perception may be required to confirm that PIPD appears to have acceptable tolerability.

This study establishes PIPD as a robust strategy for delivering fragile biologics, combining cryogenic preservation with kinetic precision to overcome the limitations of conventional methods. The integration of EV-mediated tissue reprogramming highlights its potential to accelerate healing while minimizing scarring, a critical advancement for precision medicine. Future work will focus on clinical translation and payload diversification to unlock broader therapeutic applications.

Psoriasis is a typical chronic inflammatory disease characterized by abnormal keratinocyte hyperproliferation and hyperkeratosis, leading to significant challenges in drug delivery due to the abnormally thickened epidermis and impaired barrier function [52]. The PIPD system incorporating EVs has the potential to enhance skin penetration efficiency and contribute to the modulation of excessive inflammatory and immune responses associated with the disease.

Ocular delivery presents a significant challenge to researchers due to the complex surface conditions and multiple barriers in the eye that prevent drug penetration [53,54]. Recently, jet temperature control-based cooling anesthesia technologies have been developed to assist intravitreal injections and improve patient comfort [55]; however, practical ocular delivery technologies targeting the cornea and other ocular structures are still lacking. PIPD, with its non-contact and

physical penetration properties, enables efficient drug delivery to the cornea, which serves as a barrier to hydrophilic and lipophilic drugs. Additionally, the tiny and evenly dispersed drug particles contribute to minimizing damage during drug action and delivery.

4. Conclusion

In this study, a novel transdermal drug delivery system, PIPD, utilizing high-speed cryogenic jet-induced micro ice particles, is first introduced as an effective transdermal delivery method. High-speed camera analysis showed the unprecedented unit delivery volume of 1 pL by the PIPD. Particle analysis, zeta potential measurements, and the distribution of EVs confirmed its intact integrity by PIPD, thanks to the rapid freezing and thawing processes. In vivo experiments showed the superiority of PIPD in the homogeneity of drug distribution and the amount of drug delivered in the skin layers. This superior delivery by PIPD was further confirmed by in vivo studies on mice with atopic dermatitis and wound lesions. Notable therapeutic improvements were observed in erythema, hemorrhage, scarring, and dryness in the mouse treated with PIPD.

5. Materials and methods

5.1. PIPD device and operational parameters

Picoliter ice particle delivery (PIPD) was performed using a prototype drug delivery system developed by RecensMedical, Inc. The device was equipped with a nozzle featuring an orifice diameter of 150 μm. During operation, liquid carbon dioxide was supplied at a pressure of 60 bar, expanded at the exit of the nozzle orifice, and produced a high-speed cryogenic jet. The temperature of such jet was controlled by heating the liquid CO2 before the adiabatic expansion at the nozzle to maintain the surface temperature above −4 °C. The mass flow rate of the cryogenic jet was maintained at 0.36 g/s, while the liquid drug solution was delivered at a flow rate of 500 μL/min through the central channel. The nozzle was positioned at a fixed distance of 10 mm from the target surface throughout all experiments and the EVs were in liquid form.

5.2. Drug ice particle analysis

The produced ice particles were analyzed using a high-speed camera (i-speed 514, iX Cameras, England) equipped with an ultra-macro lens (LAOWA 25 mm f/2.8 2.5-5× Ultra Macro, Laowa, South Korea) set to a magnification of 5:1 and a shutter speed of 750 ns. The particle sizes and velocities were measured in ImageJ software (National Institutes of Health, USA) using images captured within the 6–9 mm range. Calibration was performed to account for the magnification of the macro lens, ensuring accurate size measurements. The velocity of the particles was determined by measuring the trace length left in the images during the camera's shutter open time and dividing it by the exposure time. A total of 350 particles within a 2.5 mm radius from the center of the jet were analyzed to ensure a reliable trend.

5.3. Fabrication of the gelatin model

Gelatin mixtures were prepared to study the penetration depth into a solid substrate. To simulate human transdermal conditions, 5 % (*w/v*) gelatin derived from porcine skin, type A (300 g bloom, Sigma Aldrich, USA), and 0.5 % (w/v) calcium chloride (Sigma Aldrich, China) were dissolved in distilled water at 45 °C. The gelatin solution was poured into an acrylic mold with dimensions of 50 × 20 × 3 mm and placed in a refrigerator at 4 °C for 12 h to solidify.

5.4. Evaluation of the penetration depth in the gelatin model

To observe the penetration depth, 1 % (*v*/v) carboxylated red-dyed microspheres (0.5 μm, Polysciences, USA) were mixed with distilled water. This drug was injected from a height of 10 mm while the system moved at a speed of 40 mm/s. The gelatin penetration study was performed on a copper plate with its temperature controlled at 20 °C using the Peltier modules. This temperature is lower than the internal temperature of human skin. However, as previously observed, the time required for physical penetration is much faster than the dissolution time of the drug during penetration at this scale. Therefore, the final penetration depth difference caused by drug dissolution is negligible.

5.5. Cell culture and animal experiment

Human WJ-MSCs were approved by the Institutional Review Board of Konkuk University (7001355–202,010-BR-407). WJ-MSCs were cultured using CoreMAX MSC XF-UC (Corecell). Human keratinocytes (HaCaT), human dermal fibroblasts (HDF), and mouse microphage (RAW 264.7) were cultured in Dubecco's Modified Eagle Medium (DMEM; Welgene) supplemented with 10 % fetal bovine serum (FBS, USA) and 1× penicillin/streptomycin (P/S; 100 units/mL and 100 μg/mL; Gibco, USA). The cells were maintained at 37 °C in a humidified atmosphere with 5 % CO_2. BALB/c mice (female, 6 weeks old, weighing approximately 20 ± 2 g) were purchased from Orient Bio Animal Center (Seongnam City, South Korea). All animal experiments were conducted with approval from the Konkuk University Institutional Animal Care and Use Committee (IACUC #KU24032 and #KU24033). The mice were housed in a well-ventilated room under controlled temperature and humidity with a 12 h light/12 h dark cycle for one week prior to experiments. Food and water were provided ad libitum throughout the study.

5.6. EV isolation and purification

The stem cell-derived EVs were produced by StemExOne, Inc., according to the company's mass production process [56]. Briefly, the WJ-MSCs were seeded in AggreWell plates (STEMCELL Technologies) and incubated for 24 h to form spheroids. The spheroids were transferred to an Erlenmeyer flask (Corning) and cultured in RoosterCellect-EV-CC medium (RoosterBio) with 1 % P/S, 10 ng/mL TGF-β3 (Proteintech) on a rotary shaker at 60 rpm for four days at 37 °C in a humidified atmosphere with 5 % CO_2. After spheroid culture, the supernatant was collected and centrifuged at 2, 000 x*g* for 10 min to remove cell debris. The resulting supernatant was filtered through a 0.22-μm membrane filter (Millipore) and concentrated using a hollow fiber modified polyethersulfone (mPES) membrane filter column with a molecular weight cut-off of 100 kDa. Concentration was performed using a KR2i tangential flow filtration (TFF) system (Repligen, USA).

5.7. Characterization of EVs before and after PIPD

The size and zeta potential of EVs were analyzed using a nanoparticle tracking analyzer (NTA) using the ZetaView (TWIN PMX-220, Particle Metrix, Germany). Measurements were performed under the following conditions: particle count per frame (150–200), frame rate (30 frames/s), camera sensitivity (80), shutter speed (100), and temperature (25 °C). The morphology and structure of EVs were examined using a transmission electron microscope (TEM, JEM-1011, JEOL, Tokyo, Japan) operated at 80 kV and equipped with a MegaView III CCD camera (Soft Imaging System, Germany). For negative staining, 5 × 10^7 EVs were loaded onto Formvar/carbon-coated copper grids (300 mesh; FCF300-CU) and incubated for 1 min. The grids were stained with 5 μL of 1 % uranyl acetate (ThermoFisher) for 1 min, and excess stain was removed with filter paper before air drying.

5.8. Western blot and flow cytometry

The whole cell lysate (WCL) from WJ-MSC pellets and mouse tissue

were lysed in RIPA buffer (LPS solution, Korea) supplemented with protease and phosphatase inhibitor cocktail (ThermoFisher). Protein concentrations of EVs, WCL, and mouse tissues were measured using the BCA protein assay kit (ThermoFisher), following the manufacturer's protocol. Proteins were separated from 4 to 12 % Bis-Tris Flus gels (Invitrogen) and transferred to a nitrocellulose membrane (Invitrogen). The membranes were blocked with a blocking buffer (Thermo Fisher) for 10 min at RT and incubated overnight with primary antibodies at 4 °C on a rocker. After washing, the membranes were incubated with secondary antibodies for 2 h at RT. Protein signals were detected using the enhanced chemiluminescence (ECL; Thermo Fisher) kit and visualized using the iBright™ imaging system (Invitrogen). Data analysis was performed using iBright analysis software. The antibody lists used in this study are provided in Supplementary Table 1. Flow cytometry analysis was conducted using the MACSPlex Exosome Kit (Miltenyi Biotec) according to the manufacturer's protocol. The EVs were analyzed on a CytoFLEX flow cytometer (Beckman Coulter). Data acquisition and analysis were performed using CytExpert software.

5.9. Cell viability

The HDF and HaCaT cells were seeded in a 96-well plate (SPL) at a density of 3×10^3 cells per well and incubated at 37 °C in a humidified atmosphere with 5 % CO_2 for 24 h. After incubation, the cells were washed thrice with 1× PBS (Gibco), and the culture medium was replaced with DMEM (Gibco) supplemented with a 10 % EV-depleted FBS. The EVs were added to the medium at concentrations of 1×10^6, 1×10^7, 1×10^8, and 1×10^9 particles/mL. After an additional 24 h of incubation under the same conditions, cell viability was assessed using the Cellrix® assay kit (MediFab). The assay was performed according to the manufacturer's instructions by incubating the cells with the reagent for 2 h, followed by the measurement of absorbance at 450 nm using a SpectraMax iD3 microplate reader (Molecular Devices).

5.10. EV labeling and tracing

The EVs were labeled with DiR dye (Invitrogen) at RT for 1 h, and the unbound free dye was removed using OptiPrep™ (iodixanol) density gradient ultracentrifugation at 120,000 *g* for 2 h. For in vitro tracing, the DiR-labeled EVs were incubated with HDF and HaCaT cells for 12 h, after which the cells were mounted using VECTASHIELD® Antifade Mounting Medium with DAPI (Vector Laboratories), following the manufacturer's protocol. For the in vivo penetration experiment, the mice were randomly divided into four groups based on the EV administration methods: non-treated control, topical, injection, and PIPD. After 24 h, the mice were sacrificed, and dorsal skin tissue was excised and fixed in 4 % paraformaldehyde (PFA). The fixed tissues were embedded in OCT compound within cryomolds on crushed ice and snap-frozen on a cold block at −80 °C or in liquid nitrogen. Cryosections of 5-μm thickness were prepared, stained with DAPI, and analyzed using confocal laser microscopy (Carl Zeiss LSM 800) to assess EV penetration into the skin.

5.11. NO assay

RAW264.7 cells were seeded onto a 24-well plate (SPL) at a density of 1.5×10^5 cells per well and incubated at 37 °C in a humidified atmosphere with 5 % CO_2 for 12 h. After incubation, the cells were treated with a DMEM medium containing 10 % EV-depleted FBS, EVs at concentrations of 1×10^8 or 1×10^9 particles/mL, 10 ng/mL lipopolysaccharide (LPS; Sigma), and 10 μM dexamethasone (DEX; Peprotech). For NO measurement, the culture medium was harvested, centrifuged at 200 ×*g* for 3 min at RT, and the supernatant was carefully transferred into a new tube. An equal volume of Griess reagent [0.1 % N-(1-naphthyl) ethylenediamine dihydrochloride and 1 % sulfanilamide in 5 % phosphoric acid] was added to the supernatant, mixed thoroughly, and incubated at RT for 10 min. The absorbance was measured at 540 nm using a SpectraMax microplate reader (Molecular Devices).

5.12. Quantitative real-time PCR (qRT-PCR)

The total RNA was isolated from RAW264.7 cells using a Labozol reagent (Cosmo Gentech) according to the manufacturer's protocol. The purified RNA was quantified using the NanoDrop spectrophotometer (ND-ONE, NanoDrop Technologies Inc.). cDNA was synthesized from 2 μg of the total extracted RNA using an M-MuLV reverse transcription kit (Cosmo Genetech). qRT-PCR was performed using EzAmp™ qPCR 2× Master Mix (ELPIS-BIOTECH) according to the manufacturer's recommendations and run on a QuantStudio™ 3 Real-Time PCR System (Thermo Fisher Scientific). The results were normalized to GAPDH expression as an internal control and quantified using the ΔΔCt method. The primer sequences used in this study are listed in Supplementary Table 2.

5.13. In vivo wound healing assay

To analyze the in vivo wound healing capacity, the mice were injected with 60 mg/kg alfaxalone (Alfaxan, Careside, South Korea) and 10 mg/kg Rompun (4:1 ratio) for anesthesia. To induce two full-thickness skin wounds, a sterile biopsy punch (8-mm diameter, Kai Industries, Japan) was used on their backs. The mice were randomly divided into five groups ($n = 5$ per group): (1) 1× PBS control, (2) Topical application of 500 μL, (3) Injection of 500 μL, and (4) PIPD of 500 μL. The EVs were suspended in 1× PBS at a concentration of 1×10^{10} particles/mL in a volume of 500 μL. For the control and injection groups, 500 μL of the respective solutions (1× PBS only for the control group) were administered via intradermal injection at five points equidistant around each wound. The topical group treated 500 μL of the EVs suspension applied directly to the wound area. The PIPD group treated the EVs suspension applied to the wound area via PIPD. The wound size was measured at baseline (day 0) and subsequently on days 3, 5, 7, and 11 using a ruler. Wound contraction and re-epithelialization were quantified using the ImageJ software. Sections of 5 μm thickness were stained with H&E, and MT staining was performed to assess the extracellular matrix (ECM) deposition in the regenerating wound tissue.

5.14. Histological analysis

To evaluate histological evaluation, dorsal skin was fixed in 4 % PFA. Then it was embedded in paraffin, followed by sectioning. Sections of 5 μm thickness were stained with H&E, and MT staining was performed to assess ECM deposition in the regenerating wound tissue. Wound contraction and re-epithelialization were quantified using the ImageJ software. Atopic tissues were embedded in paraffin, sectioned, and stained with H&E and toluidine blue. Images were analyzed using iViewer software (UNIC Technologies). Mast cells and eosinophils were counted in three fields per sample.

5.15. In vivo atopic dermatitis

To induce atopic dermatitis-like lesions, mice were sensitized topically with 2 % DNCB on days 1 and 5, followed by 0.2 % DNCB twice weekly for two weeks. The mice were randomly assigned groups, following the same experimental design as the wound healing model. The therapeutic efficacy was assessed by weekly macroscopic evaluations. The dermatitis severity scoring system encompassed three clinical parameters: erythema/hemorrhage, scarring/dryness, and scaling/erosion, each graded on a 0–3 scale. Three weeks post-induction, the mice were sacrificed for analysis.

5.16. Statistical

All statistical analyses were performed using GraphPad Prism (version 10). Most experiments were performed in triplicate. The adjusted *p*-values were calculated using one-way or two-way ANOVA to determine the statistical significance. In all figures, the asterisk symbol indicates statistical significance as follows: *$p < 0.05$; **$p < 0.01$; ***$p < 0.001$; ****$p < 0.0001$; ####$p < 0.0001$.

CRediT authorship contribution statement

Hyunjoon Son: Writing – original draft, Conceptualization, Project administration, Methodology, Investigation, Formal analysis, Data curation, Visualization, Validation. **Sejong Kim:** Writing – original draft, Conceptualization, Project administration, Methodology, Investigation, Formal analysis, Data curation, Visualization, Validation. **Kyung Min Lim:** Investigation, Methodology, Formal analysis. **Daejin Kim:** Investigation, Validation, Formal analysis. **Kwonwoo Song:** Investigation, Data curation. **Myeongjin Song:** Investigation, Validation. **Youngseo Lee:** Investigation, Validation. **Sujin Yu:** Investigation. **Daehyun Kim:** Investigation. **Ssang-Goo Cho:** Project administration, Supervision, Conceptualization, Writing – review & editing, Resources, Funding acquisition. **Gun-Ho Kim:** Project administration, Supervision, Conceptualization, Writing – review & editing, Resources, Funding acquisition.

Declaration of competing interest

The authors declare no conflicts of interest.

Acknowledgments

This work was supported by the National Research Foundation of Korea (NRF) grant funded by the Korea government (MSIT) (2021R1A2C2014512). This study was supported by a Korean Fund for Regenerative Medicine (KFRM) grant funded by the Korean government (Ministry of Science and ICT and Ministry of Health & Welfare; grant numbers: 24A0203L1 and 25B0101L1). This work was supported by the Technology Innovation Program (20022874, Supersonic jet of cryogenic micro particles for non-invasive transdermal drug delivery) funded By the Ministry of Trade Industry & Energy (MOTIE, Korea). This paper was supported by Konkuk University in 2025.

Appendix A. Supplementary data

Supplementary data to this article can be found online at https://doi.org/10.1016/j.jconrel.2025.114184.

Data availability

The data supporting the results in this study are available within the paper and its Supplementary Information. The raw and analyzed data sets generated during the study are available for research purposes from the corresponding authors on reasonable request. Source data are provided with this paper.

References

[1] T.H. Baryakova, B.H. Pogostin, R. Langer, K.J. McHugh, Overcoming barriers to patient adherence: the case for developing innovative drug delivery systems, Nat. Rev. Drug Discov. 22 (5) (2023) 387–409, https://doi.org/10.1038/s41573-023-00670-0.

[2] W.Y. Jeong, M. Kwon, H.E. Choi, K.S. Kim, Recent advances in transdermal drug delivery systems: a review, Biomater Res. 25 (1) (2021) 24, https://doi.org/10.1186/s40824-021-00226-6.

[3] M.R. Prausnitz, R. Langer, Transdermal drug delivery, Nat. Biotechnol. 26 (11) (2008) 1261–1268, https://doi.org/10.1038/nbt.1504.

[4] M. Cui, M. Zheng, C. Wiraja, S.W.T. Chew, A. Mishra, V. Mayandi, et al., Ocular delivery of predatory Bacteria with Cryomicroneedles against eye infection, Adv Sci (Weinh). 8 (21) (2021) e2102327, https://doi.org/10.1002/advs.202102327.

[5] H. Chang, S.W.T. Chew, M. Zheng, D.C.S. Lio, C. Wiraja, Y. Mei, et al., Cryomicroneedles for transdermal cell delivery, Nat. Biomed. Eng. 5 (9) (2021) 1008–1018, https://doi.org/10.1038/s41551-021-00720-1.

[6] J.C. Yu, J.Q. Wang, Y.Q. Zhang, G.J. Chen, W.W. Mao, Y.Q. Ye, et al., Glucose-responsive insulin patch for the regulation of blood glucose in mice and minipigs, Nat. Biomed. Eng. 4 (5) (2020) 499–506, https://doi.org/10.1038/s41551-019-0508-y.

[7] S. Wang, C. Yang, W. Zhang, S. Zhao, J. You, R. Cai, et al., Glucose-responsive microneedle patch with high insulin loading capacity for prolonged Glycemic control in mice and minipigs, ACS Nano (2024), https://doi.org/10.1021/acsnano.4c05562.

[8] S. Kim, H. Yang, J. Eum, Y. Ma, S. Fakhraei Lahiji, H. Jung, Implantable powder-carrying microneedles for transdermal delivery of high-dose insulin with enhanced activity, Biomaterials 232 (2020) 119733, https://doi.org/10.1016/j.biomaterials.2019.119733.

[9] J. Schramm-Baxter, S. Mitragotri, Needle-free jet injections: dependence of jet penetration and dispersion in the skin on jet power, J. Control. Release 97 (3) (2004) 527–535, https://doi.org/10.1016/j.jconrel.2004.04.006.

[10] A. Mohizin, J.K. Kim, Conceptualisation of a novel electromechanical system for small-volume needle-free jet injection, Eng. Appl. Comput. Fluid Mech. 17 (1) (2023), https://doi.org/10.1080/19942060.2023.2240868.

[11] Y. Miyazaki, M. Usawa, S. Kawai, J. Yee, M. Muto, Y. Tagawa, Dynamic mechanical interaction between injection liquid and human tissue simulant induced by needle-free injection of a highly focused microjet, Sci. Rep. 11 (1) (2021) 14544, https://doi.org/10.1038/s41598-021-94018-6.

[12] J. Schoppink, Rivas D. Fernandez, Jet injectors: perspectives for small volume delivery with lasers, Adv. Drug Deliv. Rev. 182 (2022) 114109, https://doi.org/10.1016/j.addr.2021.114109.

[13] H. Yu, S. Yang, J. Hu, H. Wang, CFD study of gas-powder injection characteristics in a novel lance with supersonic shrouding jet, Chem. Eng. J. (2024) 481, https://doi.org/10.1016/j.cej.2023.148470.

[14] C.Y. Li, Z.W. Wang, C. Tu, J.B. Wang, B.Q. Jiang, Q. Li, et al., Needle-free injection of insulin powder: delivery efficiency and skin irritation assessment, J Zhejiang Univ Sci B 15 (10) (2014) 888–899, https://doi.org/10.1631/jzus.B1400065.

[15] M. Kendall, T. Mitchell, P. Wrighton-Smith, Intradermal ballistic delivery of micro-particles into excised human skin for pharmaceutical applications, J. Biomech. 37 (11) (2004) 1733–1741, https://doi.org/10.1016/j.jbiomech.2004.01.032.

[16] S. Guo, Z. Liu, Y. Zhang, J. Wang, Z. Gao, J. Gong, Microdroplet cryo-crystallization for producing budesonide microparticles with optimized physicochemical properties, Particuology 103 (2025) 128–140, https://doi.org/10.1016/j.partic.2025.05.014.

[17] H. Ham, J.J. Yoh, A liquid breakdown driven non-invasive microjet injection system, Med. Eng. Phys. 92 (2021) 54–63, https://doi.org/10.1016/j.medengphy.2021.05.002.

[18] S. Somasundaram, A.A.O. Tay, A study of intermittent liquid nitrogen sprays, Appl. Therm. Eng. 69 (1–2) (2014) 199–207, https://doi.org/10.1016/j.applthermaleng.2013.11.066.

[19] B. Li, J. Wang, J. Tian, B. Chen, H. Xu, H. Jia, Transient cooling performance of R134a flash-evaporation spray enhanced by cold air jet: a novel heat transfer enhancement method in laser dermatology, Int. J. Heat Mass Transf. (2022) 199, https://doi.org/10.1016/j.ijheatmasstransfer.2022.123468.

[20] C.W. Visser, P.E. Frommhold, S. Wildeman, R. Mettin, D. Lohse, C. Sun, Dynamics of high-speed micro-drop impact: numerical simulations and experiments at frame-to-frame times below 100 ns, Soft Matter 11 (9) (2015) 1708–1722, https://doi.org/10.1039/c4sm02474e.

[21] N.T. Weissmueller, L. Marsay, H.A. Schiffter, R.C. Carlisle, C.S. Rollier, R. K. Prud'homme, et al., Alternative vaccine administration by powder injection: needle-free dermal delivery of the glycoconjugate meningococcal group Y vaccine, PLoS One 12 (8) (2017) e0183427, https://doi.org/10.1371/journal.pone.0183427.

[22] W. van Hoeve, S. Gekle, J.H. Snoeijer, M. Versluis, M.P. Brenner, D. Lohse, Breakup of diminutive Rayleigh jets, Phys. Fluids 22 (12) (2010), https://doi.org/10.1063/1.3524533.

[23] K.O. Fong, X. Xue, R. Osuna-Orozco, A. Aliseda, Gas–liquid coaxial atomization with swirl in high-pressure environments, Int. J. Multiphase Flow (2024) 174, https://doi.org/10.1016/j.ijmultiphaseflow.2024.104767.

[24] Y. Zhang, Y. Tian, J. Le, Review of atomization characteristics of liquid jets in crossflow, Phys. Fluids 36 (2) (2024), https://doi.org/10.1063/5.0191630.

[25] G. Ohlsson, S.R. Tabaei, J. Beech, J. Kvassman, U. Johanson, P. Kjellbom, et al., Solute transport on the sub 100 ms scale across the lipid bilayer membrane of individual proteoliposomes, Lab Chip 12 (22) (2012) 4635–4643, https://doi.org/10.1039/c2lc40518k.

[26] C.B. Wilson, W.M. Yau, R. Tycko, Experimental evidence for millisecond-timescale structural evolution following the microsecond-timescale folding of a small protein, Phys. Rev. Lett. 132 (4) (2024) 048402, https://doi.org/10.1103/PhysRevLett.132.048402.

[27] T.J. Mitchell, M.A.F. Kendall, B.J. Bellhouse, A ballistic study of micro-particle penetration to the oral mucosa, Int. J. Impact Eng. 28 (6) (2003) 581–599, https://doi.org/10.1016/s0734-743x(02)00150-1.

[28] O.A. Shergold, N.A. Fleck, Experimental investigation into the deep penetration of soft solids by sharp and blunt punches, with application to the piercing of skin, J. Biomech. Eng. 127 (5) (2005) 838–848, https://doi.org/10.1115/1.1992528.

[29] V. Menezes, S. Kumar, K. Takayama, Shock wave driven liquid microjets for drug delivery, J. Appl. Phys. 106 (8) (2009), https://doi.org/10.1063/1.3245320.
[30] T. Kato, T. Arafune, T. Washio, A. Nakagawa, Y. Ogawa, T. Tominaga, et al., Mechanics of the injected pulsejet into gelatin gel and evaluation of the effect by puncture and crack generation and growth, J. Appl. Phys. 116 (7) (2014), https://doi.org/10.1063/1.4893175.
[31] Y. Tagawa, N. Oudalov, A. El Ghalbzouri, C. Sun, D. Lohse, Needle-free injection into skin and soft matter with highly focused microjets, Lab Chip 13 (7) (2013) 1357–1363, https://doi.org/10.1039/c2lc41204g.
[32] M. Kendall, S. Rishworth, F. Carter, T. Mitchell, Effects of relative humidity and ambient temperature on the ballistic delivery of micro-particles to excised porcine skin, J. Invest. Dermatol. 122 (3) (2004) 739–746, https://doi.org/10.1111/j.0022-202X.2004.22320.x.
[33] W. Yang, V.R. Sherman, B. Gludovatz, E. Schaible, P. Stewart, R.O. Ritchie, et al., On the tear resistance of skin, Nat. Commun. 6 (2015) 6649, https://doi.org/10.1038/ncomms7649.
[34] A. Pissarenko, W. Yang, H. Quan, K.A. Brown, A. Williams, W.G. Proud, et al., Tensile behavior and structural characterization of pig dermis, Acta Biomater. 86 (2019) 77–95, https://doi.org/10.1016/j.actbio.2019.01.023.
[35] W. Zhu, T. Wei, Y. Xu, Q. Jin, Y. Chao, J. Lu, et al., Non-invasive transdermal delivery of biomacromolecules with fluorocarbon-modified chitosan for melanoma immunotherapy and viral vaccines, Nat. Commun. 15 (1) (2024) 820, https://doi.org/10.1038/s41467-024-45158-6.
[36] D.C.S. Lio, R.N. Chia, M.S.Y. Kwek, C. Wiraja, L.E. Madden, H. Chang, et al., Temporal pressure enhanced topical drug delivery through micropore formation, Sci. Adv. 6(22):eaaz6919 (2020), https://doi.org/10.1126/sciadv.aaz6919.
[37] W. Hu, W. Wang, Z. Chen, Y. Chen, Z. Wang, Engineered exosomes and composite biomaterials for tissue regeneration, Theranostics 14 (5) (2024) 2099–2126, https://doi.org/10.7150/thno.93088.
[38] H.I. Kim, J. Park, Y. Zhu, X. Wang, Y. Han, D. Zhang, Recent advances in extracellular vesicles for therapeutic cargo delivery, Exp. Mol. Med. 56 (4) (2024) 836–849, https://doi.org/10.1038/s12276-024-01201-6.
[39] K. Song, A.A. Dayem, S. Lee, Y. Choi, K.M. Lim, S. Kim, et al., Superior therapeutic activity of TGF-beta-induced extracellular vesicles against interstitial cystitis, J. Control. Release 348 (2022) 924–937, https://doi.org/10.1016/j.jconrel.2022.06.045.
[40] M. Takenaka, A. Yabuta, Y. Takahashi, Y. Takakura, Interleukin-4-carrying small extracellular vesicles with a high potential as anti-inflammatory therapeutics based on modulation of macrophage function, Biomaterials 278 (2021) 121160, https://doi.org/10.1016/j.biomaterials.2021.121160.
[41] T.Y. Gil, Y.M. Kang, Y.J. Eom, C.H. Hong, H.J. An, Anti-atopic dermatitis effect of seaweed Fulvescens extract via inhibiting the STAT1 pathway, Mediat. Inflamm. 2019 (2019) 3760934, https://doi.org/10.1155/2019/3760934.
[42] F. Peng, J. Zong, T. Zhao, P. Shi, M. Lu, X. Qu, et al., Anti-inflammatory and immunomodulatory effects of polysaccharide extracted from Wuguchong (maggot) on 2,4-dinitrochlorobenzene-induced atopic dermatitis in mice, Front. Pharmacol. 14 (2023) 1119103, https://doi.org/10.3389/fphar.2023.1119103.
[43] T. Liu, J. Hao, H. Lei, Y. Chen, L. Liu, L. Jia, et al., Recombinant collagen for the repair of skin wounds and photo-aging damage. Regenerative, Biomaterials (2024) 11, https://doi.org/10.1093/rb/rbae108.
[44] S.P. Mihindukulasooriya, H.J. Kim, J. Cho, K.H.I.N. Madushani Herath, J. Yang, D. T.T. Dinh, et al., Polyphenol-rich Sargassum horneri alleviates atopic dermatitis-like skin lesions in NC/Nga mice by suppressing Th2-mediated cytokine IL-13, Algae 37 (4) (2022) 331–347, https://doi.org/10.4490/algae.2022.37.11.24.
[45] J.C.J. Wei, G.A. Edwards, D.J. Martin, H. Huang, M.L. Crichton, M.A.F. Kendall, Allometric scaling of skin thickness, elasticity, viscoelasticity to mass for micro-medical device translation: from mice, rats, rabbits, pigs to humans, Sci. Rep. 7 (1) (2017) 15885, https://doi.org/10.1038/s41598-017-15830-7.
[46] M.D. Lynch, F.M. Watt, Fibroblast heterogeneity: implications for human disease, J. Clin. Invest. 128 (1) (2018) 26–35, https://doi.org/10.1172/JCI93555.
[47] D. Kocsis, V. Klang, E.M. Schweiger, Z. Varga-Medveczky, A. Mihaly, C. Pongor, et al., Characterization and ex vivo evaluation of excised skin samples as substitutes for human dermal barrier in pharmaceutical and dermatological studies, Skin Res. Technol. 28 (5) (2022) 664–676, https://doi.org/10.1111/srt.13165.
[48] J.A. Bouwstra, A. Nadaban, W. Bras, C. McCabe, A. Bunge, G.S. Gooris, The skin barrier: An extraordinary interface with an exceptional lipid organization, Prog. Lipid Res. 92 (2023) 101252, https://doi.org/10.1016/j.plipres.2023.101252.
[49] S.A. Ranamukhaarachchi, S. Lehnert, S.L. Ranamukhaarachchi, L. Sprenger, T. Schneider, I. Mansoor, et al., A micromechanical comparison of human and porcine skin before and after preservation by freezing for medical device development, Sci. Rep. 6 (2016) 32074, https://doi.org/10.1038/srep32074.
[50] M.F. Griffin, B.C. Leung, Y. Premakumar, M. Szarko, P.E. Butler, Comparison of the mechanical properties of different skin sites for auricular and nasal reconstruction, J. Otolaryngol. Head Neck Surg. 46 (1) (2017) 33, https://doi.org/10.1186/s40463-017-0210-6.
[51] G.S. Chuang, W. Farinelli, R.R. Anderson, Selective Cryolysis of melanocytes: critical temperature and exposure time to induce selective pigmentary loss in Yucatan pig skin, Lasers Surg. Med. 53 (7) (2021) 978–985, https://doi.org/10.1002/lsm.23372.
[52] M. Song, K.M. Lim, K. Song, G.H. Kang, S.J. Kim, Y. Lee, et al., Efficient treatment of psoriasis using conditioned media from mesenchymal stem cell spheroids cultured to produce transforming growth factor-beta1-enriched small-sized extracellular vesicles, Int J Stem Cells. 17 (4) (2024) 407–417, https://doi.org/10.15283/ijsc24089.
[53] A. Bhattacharjee, P.J. Das, P. Adhikari, D. Marbaniang, P. Pal, S. Ray, et al., Novel drug delivery systems for ocular therapy: with special reference to liposomal ocular delivery, Eur. J. Ophthalmol. 29 (1) (2019) 113–126, https://doi.org/10.1177/1120672118769776.
[54] N.S. Kulkarni, A. Josowitz, R. James, Y. Liu, B. Rayaprolu, B. Sagdullaev, et al., Latest trends & strategies in ocular drug delivery, Methods 235 (2025) 100–117, https://doi.org/10.1016/j.ymeth.2025.02.003.
[55] D.L. Chao, N.T. Rinella, A.M. Khanani, C.C. Wykoff, G.H. Kim, Cooling Anesthesia for intravitreal injection: results of the prospective open-label, dose-ranging COOL-1 trial, Clin. Ophthalmol. 15 (2021) 4659–4666, https://doi.org/10.2147/OPTH.S336653.
[56] K. Min Lim, S. Kim, J. Yeom, Y. Choi, Y. Lee, J. An, et al., Advanced 3D dynamic culture system with transforming growth factor-beta3 enhances production of potent extracellular vesicles with modified protein cargoes via upregulation of TGF-beta signaling, J. Adv. Res. 47 (2023) 57–74, https://doi.org/10.1016/j.jare.2022.09.005.